

ARTICLE

Received 17 Jun 2015 | Accepted 22 Oct 2015 | Published 24 Nov 2015

DOI: 10.1038/ncomms9985

OPEN

Giant elastic tunability in strained BiFeO₃ near an electrically induced phase transition

Q. Li^{1,*}, Y. Cao^{1,*}, P. Yu^{2,3}, R.K. Vasudevan¹, N. Laanait¹, A. Tselev¹, F. Xue⁴, L.Q. Chen⁴, P. Maksymovych¹, S.V. Kalinin¹ & N. Balke¹

Elastic anomalies are signatures of phase transitions in condensed matters and have traditionally been studied using various techniques spanning from neutron scattering to static mechanical testing. Here, using band-excitation elastic/piezoresponse spectroscopy, we probed sub-MHz elastic dynamics of a tip bias-induced rhombohedral – tetragonal phase transition of strained (001)-BiFeO₃ (rhombohedral) ferroelectric thin films from $\sim 10^3$ nm³ sample volumes. Near this transition, we observed that the Young's modulus intrinsically softens by over 30% coinciding with two- to three-fold enhancement of local piezoresponse. Coupled with phase-field modelling, we also addressed the influence of polarization switching and mesoscopic structural heterogeneities (for example, domain walls) on the kinetics of this phase transition, thereby providing fresh insights into the morphotropic phase boundary in ferroelectrics. Furthermore, the giant electrically tunable elastic stiffness and corresponding electromechanical properties observed here suggest potential applications of BiFeO₃ in next-generation frequency-agile electroacoustic devices, based on the utilization of the soft modes underlying successive ferroelectric phase transitions.

¹Center for Nanophase Materials Sciences and Institute for Functional Imaging of Materials, Oak Ridge National Laboratory, Oak Ridge, Tennessee 37831, USA. ²State Key Laboratory for Low-Dimensional Quantum Physics, Department of Physics and Collaborative Innovation Center for Quantum Matter, Tsinghua University, Beijing 100084, China. ³RIKEN Center for Emergent Matter Science (CEMS), Wako, Saitama 351-0198, Japan. ⁴Department of Materials Science and Engineering, Pennsylvania State University, University Park, Pennsylvania 16802, USA. * These authors contributed equally to this work. Correspondence and requests for materials should be addressed to N.B. (email: balken@ornl.gov).

Ferroelectrics underpin a vast spectrum of modern technologies, including ultrasonic transducers, precision actuators, nonvolatile memories, to name a few^{1–3}. Pivotal to the continued development of ferroelectrics is a deep understanding of their structural – dynamics relationship, which is conventionally separated into lattice and domain structure levels⁴. The intrinsic lattice contribution has long been centred on the concept of morphotropic phase boundary (MPB), which describes the degeneracy/coexistence of, classically, rhombohedral (**R**) and tetragonal (**T**) phases across structural transitions driven by composition⁵, temperature⁶, applied electric (E-) field⁷, epitaxial strain^{8,9} and pressure^{10,11}. This MPB picture has been substantially refined over last two decades through the discoveries of monoclinic bridge phases^{12,13} and associated polarization (P) rotation mechanism¹⁴. At the domain level, extrinsic structural dynamics takes place via domain wall motions and contribute to many of the ferroelectric properties^{15,16}. Recent studies have also revealed that monoclinic phases can be stabilized under local stress/electric fields generated by complex domain structures in BaTiO₃ and KNbO₃ (refs 6,17), thus blurring the boundary of such structural hierarchy.

Scattering techniques based on X-ray/neutron and electron probes are capable of resolving subtleties in crystal structure and lattice dynamics near the MPBs and allow *in situ* tracking of their response to external stimuli; however, these techniques generally fall short of capabilities to correlate structural dynamics with real-space microstructures, especially regarding domain structures. To this end, piezoresponse force microscopy (PFM) has emerged as a primary tool for imaging electromechanical properties of materials with nanoscale resolution¹⁸, and PFM spectroscopy has also been developed in some forms enabling local probing of polarization switching dynamics^{19–21}. This latter issue has been the subject of extensive PFM studies, yielding significant observations of, for example, low-energy nucleation centres at ferroelastic domain walls^{20,22}. In a limited number of cases, hints of phase transition phenomena have also been reported^{9,23}.

As the most studied multiferroic compound, BiFeO₃ (BFO) shows many promising functionalities emerging from its intercoupled polarization, transport, mechanical and magnetic properties^{8,9,22,24–28}. Mixed-R/T phase BFO thin films near a strain-induced MPB (on LaAlO₃ substrates) have attracted particular interests for piezoelectric applications due to their large field-induced strains and shape-memory effects^{8,9,29–33}. These effects, though being reversible, are hysteretic (that is, the field-induced state has to be annihilated by applying an opposite field) as a consequence of the intricate mixed-phase microstructure and thus are undesirable in applications of, for example, tunable devices³. For such purpose, BFO in the stability field of R-phase is to be considered instead.

Here, we employed band-excitation³⁴ piezoresponse spectroscopy (BEPS) to probe local bias-induced R – T phase transition as well as polarization switching behaviour of strained R-BFO thin films. By deciphering the elastic spectroscopy inherent in BEPS that acts as a nanoscale analogy to macroscopic resonant ultrasound techniques³⁵, we examined the sub-MHz elastic dynamics associated with both intrinsic and extrinsic structural activities of the system. This added information channel supported by phase-field modelling allowed us to further explore the kinetic interaction between the polarization switching and heterogeneous domain structures with the R – T transition. Our results highlight giant electrically tunable elastic properties of BFO heretofore largely unappreciated.

Results

Bipolar BEPS loops. In this study, we focus on a 50 nm BiFeO₃ thin film with a bottom layer of La_{0.7}Sr_{0.3}MnO₃ grown on

(001)-SrTiO₃ (STO) substrates (cubic indices are used in this article). The as-grown BFO film comprises four essentially equally populated, upwards-polarized twin variants due to -1.5% epitaxial strains imposed by STO and certain electrical boundary conditions^{36,37}. X-ray reciprocal space mapping confirms a distorted **R** (or monoclinic **M_A** (ref. 13); Fig. 1a) average symmetry of the film with *c/a* axis ratio = 1.043. Figure 1b,c illustrates the surface morphology and corresponding vertical/lateral PFM images showing mutually orthogonal surface domain patterns in widths of ~ 100 nm and separated by largely straight boundaries. Figure 1d–h presents a typical set of single-point (out-of-plane) BEPS results acquired at the domain interior. As is readily seen from the amplitude spectrographs (Fig. 1d), the on-field response shows strong shifts in contact resonance frequency ($f_{c,r}$) during all the switching cycles, in striking contrast with the off-field response. Further details can be extracted from the derived loops: the on-field $f_{c,r}$ shifts downwards with bias in both polarities and for large bias windows, it saturates (and slightly recovers) before the maximum bias followed by a second drop when decreasing the bias thus forming characteristic hysteresis (see the branch A–C in Fig. 1f); for the off-field $f_{c,r}$ loops, only weak anomalies can be found near ± 3 V where the domain switching events occur³⁸. Similar patterns are also followed by the quality (Q)-factor loops with relatively larger variation in the off-field state (Fig. 1h).

The off-field piezoresponse loops have the canonical square shape gradually saturating under positive tip biases¹⁹ (Fig. 1g). By comparison, the on-field loops show bias-dependent, enhanced piezoresponse in accordance with the shift patterns of $f_{c,r}$; in particular, a ‘head’-like hysteretic feature forms in the positive half-cycle. Along with the $f_{c,r}$ anomalies, this feature is well reproducible in BEPS mapping across the film on average leading to two- to threefold enhancement (versus zero-bias) of piezoresponse, and its propensity appears to be weaker for the negative bias side where the applied E-field is parallel to the pristine *P* direction (Fig. 1i). Note that the measured on-field piezoresponse in these cases is truly dominated by electromechanical response over weak or no contributions from the parasite electrostatic and conduction current effects (Supplementary Note 1 and Supplementary Figs 1,2). This loop shape is also distinct from those peculiar backswitching loops mediated by charge injection, since it occurs only on-field and without any self-crossings³⁹.

In BEPS, systematic and reproducible changes in $f_{c,r}$ are due to alteration of the elastic properties of samples³⁸, as is indeed the case here. Through cantilever dynamics and contact mechanics calculations (see details in Supplementary Note 2 and Supplementary Table 1), we find that the Young’s modulus (*Y*) of the BFO film changes from ~ 204 GPa in the pristine state to, for example ~ 141 GPa at 12 V shown in Fig. 1f, where the $\Delta f_{c,r}$ peaks at ~ 4.7 kHz, amounting to a remarkable $\sim 30\%$ elastic softening. This softening behaviour can be instantaneously switched on/off by bias within the probed millisecond timescale, and remains basically unchanged when the contact resonance is driven by external mechanical excitation³⁸. Similar softening effects are also observed in the lateral/torsional BEPS mode, where in-plane polarization is detected and torsional $f_{c,r}$ reflects the shear modulus (*G*) of samples⁴⁰. Overall, the lateral piezoresponse loops of this BFO film are not well-defined in the low-bias region compared with their simultaneously acquired out-of-plane counterparts, presumably due to its complex in-plane switching behaviour; however, there is a recurring feature manifest in all the in-plane loops: as illustrated in Fig. 1j,k, the on-field piezoresponse is enhanced along with the elastic softening up to a threshold bias and then drops quickly. All these observed BEPS characteristics imply an intrinsic dynamic process taking place, reminiscent of

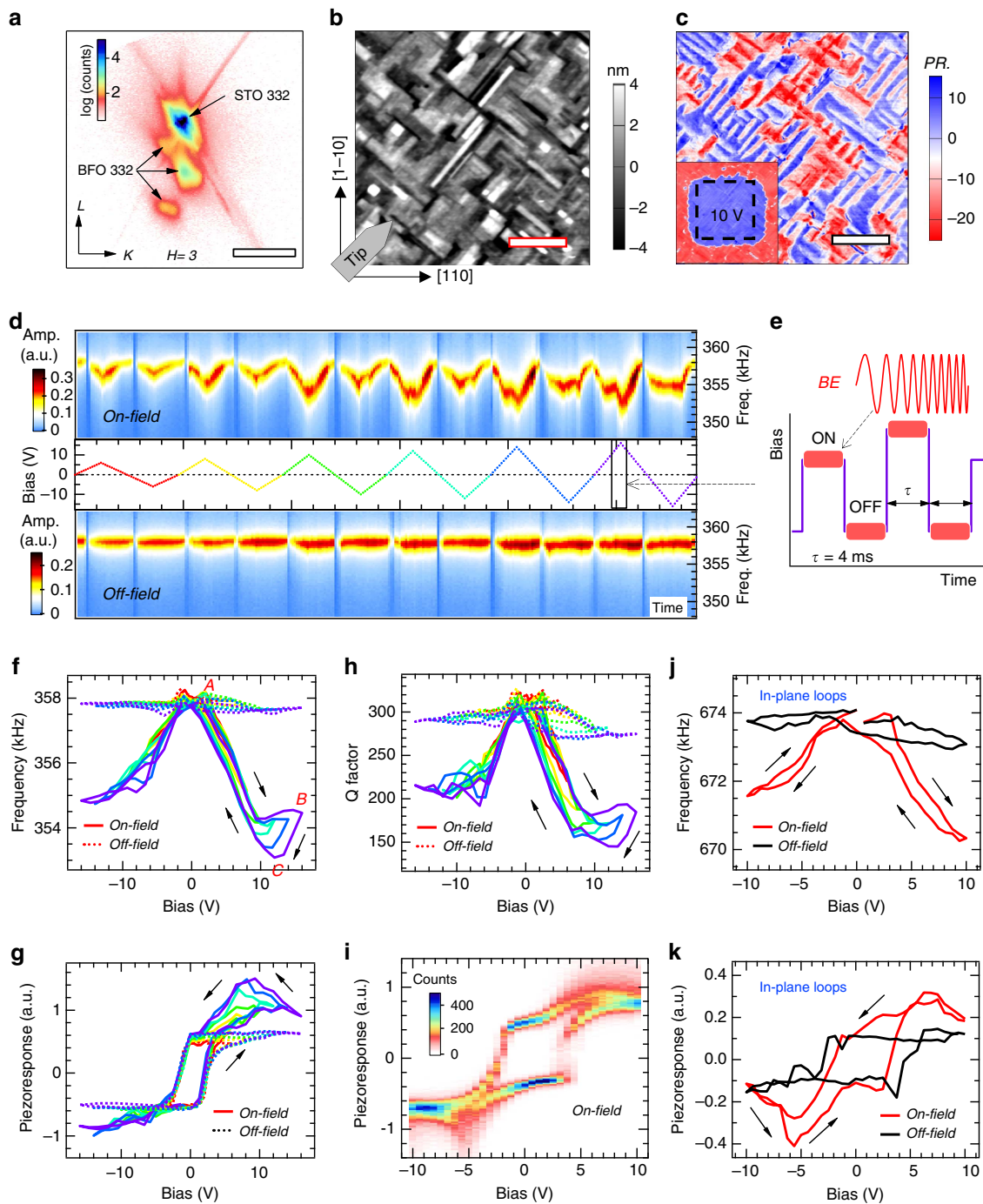


Figure 1 | Bipolar BEPS switching loops of 50 nm BFO/STO. (a) Reciprocal space map near the STO 332 reflection showing three-fold splitting indicative of a \mathbf{M}_A structure of BFO. Scale bar, $1/3.905 \text{ \AA}^{-1}$. (b,c) Morphology (b) and corresponding lateral PFM (c) images; Inset in c shows the corresponding vertical PFM image after the center square area was poled with 10 V tip bias. The cantilever alignment adopted in all BEPS measurements is shown in b. Scale bar, 1 μm . (d-h) Single-point BEPS performed under ascending bias windows as shown in d, which also illustrates the measured piezoresponse amplitude spectrographs; total time length = 2.3 s. e is a schematic representation for the chirp-type BE waveform and on/off-field d.c. switching sequences. f-h are the fitted frequency (f), piezoresponse (g) and Q factor (h) loops with their sense marked by arrows and colour coded by the bias windows shown in d. (i) Histogram of the on-field piezoresponse loops acquired from 50×50 points over a $1 \times 1 \mu\text{m}^2$ region. (j,k) Single-point in-plane BEPS frequency (j) and piezoresponse (k) loops acquired in the lateral mode with the sense marked by arrows. a.u., arbitrary unit.

the R–T phase transition of the system. The measured Y variations of the BFO/STO film are also found to be bounded by the elastic moduli of different R- or T-phase BFO samples probed at GHz frequencies by Doig *et al.*⁴¹. Note that similar frequency response and piezoresponse enhancement were also observed in (001)-BFO thin films under different epitaxial

strains (for example, BFO/DyScO₃, strain approximately -0.5% ; Supplementary Note 3 and Supplementary Fig. 3).

Phase-field modelling of a single domain. Phase-field modelling offers direct visualization of the evolution of ferroelectric

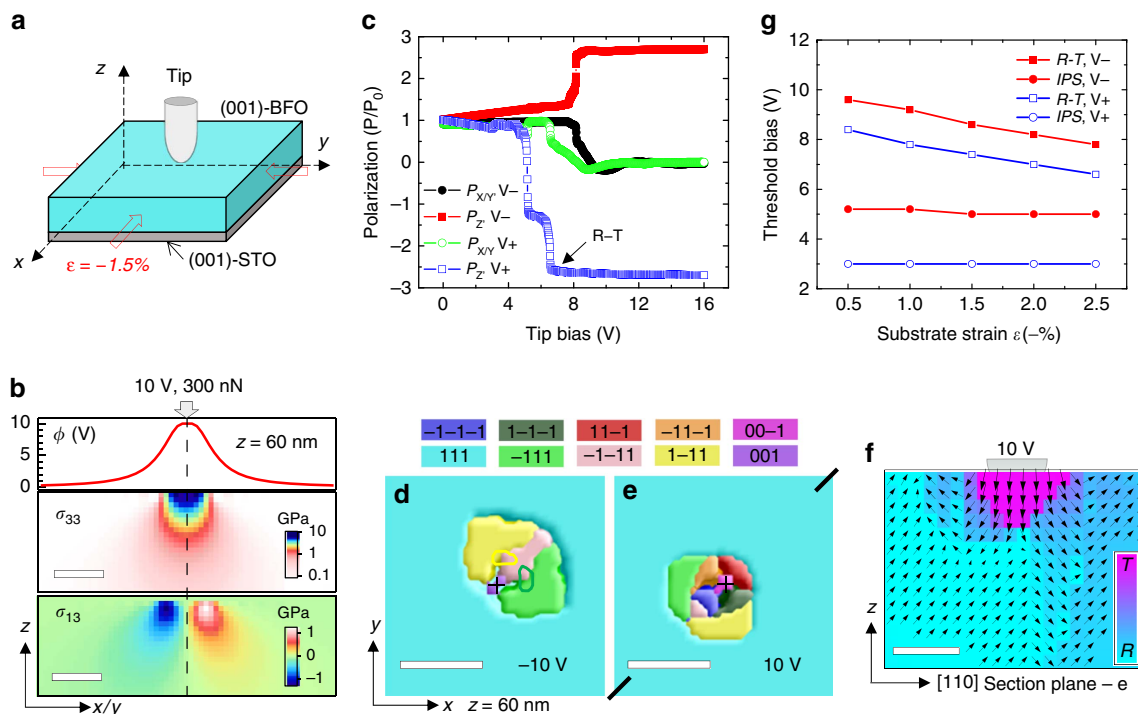


Figure 2 | Phase-field modelling of a single-domain BFO. (a) Schematic for the model geometry (not to scale): $x = y = 128$ nm, $z = 50/10$ nm, tip coordinate = (64, 64, 60) nm. Thick arrows represent the biaxial substrate strain $\varepsilon = -1.5\%$. (b) Line/plane distribution profiles of the tip potential ϕ and normal/shear stress components σ_{33}/σ_{13} under 10 V tip bias and 300 nN loading force. Scale bar, 10 nm. (c) Evolution of local polarization $P_{(x, y, z)}$ components underneath the tip during incremental application of positive (V+) and negative (V-) biases. $P_0 = 0.58$ C m $^{-2}$. (d–f) Stabilized domain/phase configurations at selected biases. In d, e, the P direction is color-coded and the tip center position marked by a cross. The outlines of the nucleated $[111]_R$ and $[\bar{1}\bar{1}\bar{1}]_R$ domains at -5 V are overlaid on d. Arrows in f show the direction of P and scale with its magnitude in size. Scale bar, 20 nm in d, e and 5 nm in f. (g) Calculated in-plane switching (IPS) and **R–T** phase transition threshold biases as a function of substrate strain.

polarization during BEPS measurements. We start from a single $[111]_R$ -domain BFO/STO model as illustrated in Fig. 2a. Here the lateral tip potential spreading is modelled as a flat-top Lorentz function, $\phi(x, y) = \phi_0 \gamma^2 / ((r - a)^2 + \gamma^2)$, $r > a$; $\phi_0, r \leq a$, where r is the distance from the tip and γ is the half width at half maximum of applied bias, ϕ_0 ; given the presence of strong tip indentation⁴², the center area with radius a , obtained self-consistently from the contact mechanics calculations, is set equipotential. Figure 2b shows the calculated depth profiles of normal and shear stresses under the tip loading force. Both types of stresses are concentrated within ~ 10 nm length scale, indicating the size of sample volume where local elasticity is effectively probed⁴⁰, approximately commensurate with that for piezoresponse. Figure 2c shows the calculated local P values underneath the tip following increasing sequences of tip bias. For both bias polarities, there are sudden jumps in P occurring within 6–10 V, after which its Z component, P_z increases to $\sim 2.7P_0$ and the P_x/P_y components reduce to zero. Such jumps signify the **R–T** phase transition and the calculated P_z faithfully reproduces the experimental P value (~ 1.5 C m $^{-2}$) of T-BFO⁴³. The fact that this transition occurs earlier by ~ 2 V along the antiparallel E-field direction (positive bias) is somewhat counterintuitive, as one may assume that the $\mathbf{M}_A - \mathbf{T}$ polarization rotation path would be ‘shorter’ in the parallel E-field condition¹⁴. This points to a competing interaction between the polarization switching and rotation processes, as the domain/phase configuration results from minimization of the system free energy with respect to the driving force, electrostatic energy – EP. The stabilized domain configurations under ± 10 V are presented, for example, in Fig. 2d–f. Noticeable in-plane switching (IPS) activities can be seen for both polarities (for positive tip biases, the IPS also

involves out-of-plane switching) due to the lateral components of tip E-fields²² (Supplementary Fig. 4 and Supplementary Note 4), leading to ~ 20 nm domain clusters with four **R**-phase twins enclosing a **T**-phase domain underneath the tip (Fig. 2d, e). In the case of 10 V, the **T**-phase extends ~ 4 nm into the film assuming a wedge-shape depth profile and around it, a thin (1 or 2 nm) transition layer with higher P than that of **R**-BFO is also visible (Fig. 2f), which could be an indicator of the **R/T** phase boundary thickness⁸. Furthermore, we considered the influence of substrate strain on the **R–T** transition as well as IPS of the **R**-phase. Here the IPS threshold bias is defined as the voltage at which nascent domains are visually detected on the surface, since they do not nucleate right below the tip (see an illustration on Fig. 2d). Within the strain range from -0.5% to -2.5% , the **R–T** threshold bias decreases monotonically as expected, while that of IPS appears almost independent of substrate strain (Fig. 2g).

In light of these modelling results, we attribute the observed BEPS features to the occurrence of the **T**-phase. Note that T-BFO is not soft *per se*, neither in terms of elasticity nor piezoelectricity⁴⁴. Therefore, the softening behaviour has to be explained by the **R/T** phase coexistence (that is, MPB) or more naturally, the **R–T** phase instability^{4,45}. Elastic softening occurs near phase transitions following specific patterns as determined by their transition characters, for example, order parameter type⁴⁶. In our case, it is more complicated because the transition is locally and non-uniformly driven; therefore, the measured dynamics is a convolution of the lattice dynamics and the growth kinetics of the emergent phase. For instance, when a **T**-phase nucleus grows outwards under higher biases, the inner region recovers as it passes through the instability field but the surrounding lattice enters that and softens overall, probably

maintaining the softening trend for the probe volume. This renders it not straightforward to assign an exact $\mathbf{R} - \mathbf{T}$ transition point to the measured elastic or piezoresponse spectra, albeit their peak softening biases compare favourably with the calculated threshold biases. In this regard, the lateral piezoresponse may be more informative, since in principle it changes most drastically during the $\mathbf{R} - \mathbf{T}$ transition.

Unipolar BEPS and strain loops. To further find links between the softening behaviour and the IPS and $\mathbf{R} - \mathbf{T}$ transition of the BFO film, we performed unipolar BEPS in the parallel E-field condition; to fulfil this, a pre-poling cycle was adopted in the positive bias case so as to create a single- P_z domain state. In contrast to the bipolar loops, most unipolar loops measured off the pristine domain boundaries are essentially non-hysteretic and undergo a continuous softening to the deepest point (as would be the point-C in Fig. 1f), followed by a recovery or hardening when the T-phase continues to grow with bias. A typical set of single-point unipolar loops are presented in Fig. 3a–f. These loops clearly illustrate two anomalies associated with both types of structural activities. The IPS occurs in the low-bias regions close to the modelling results, and in this case (and many other measured points), it is much stronger for positive tip biases as is reflected by a marked enhancement of piezoresponse (cf. Fig. 3a,d), which is also accompanied with large increases in Q^{-1} (Fig. 3b,e), the loss factor signifying internal energy dissipation, as well as in second harmonic piezoresponse (Fig. 3c,f). Previous studies have established that the second harmonic piezoresponse of ferroelectric materials mainly originates from reversible interface (domain walls and/or phase boundaries) motions under a.c. excitations^{47,48}. Therefore, all these

observations lead to a coherent picture of enhanced domain wall motions contributing extrinsically to the piezoresponse near the IPS coercive E-fields. On the other hand, the IPS seems only to cause moderate perturbation to the smooth, wide-range operating elastic softening driven by the $\mathbf{R} - \mathbf{T}$ phase instability, although it can increase the piezoresponse and energy loss to a much higher degree. This agrees with macroscopic elastic studies in which the influence of mobile twin walls appears more noticeably as damping than reduction in the apparent elastic moduli of samples in the same sub-MHz frequency range³⁵. Such difference can be greater in BEPS presumably due to its highly localized, weak excitation nature and thus the probed real part elasticity is essentially intrinsic. At the $\mathbf{R} - \mathbf{T}$ transition regions, the piezoresponse, $\Delta f_{c,r}$ and Q^{-1} all reach their maxima; however, these anomalies along with those in the phase signals are not exactly synchronized in bias, implying subtle difference in their sensitivities to structural changes. The dominant piezoresponse enhancement and dissipation mechanisms at this stage should be attributed to the intrinsic lattice softening of BFO, as is also corroborated by the weak second harmonic piezoresponse measured here that evidences insignificant interphase boundary mobility.

We also acquired static on-field strain curves simultaneously with unipolar BEPS, as illustrated by typical single-point results in Fig. 3g,h. Near the $\mathbf{R} - \mathbf{T}$ transition, the piezoelectric coefficient (d_{33}) derived from the strain curves appears basically the same as the dynamic piezoresponse probed at ~ 350 kHz within the calibration accuracy, again implying that the piezoresponse is intrinsic here. Besides that, the strains curves exhibit stronger fluctuations around the IPS region, which can be expected as a result of higher twin wall mobility under slowly varying E-fields. Figure 3i shows the histogram of d_{33} loops derived from a

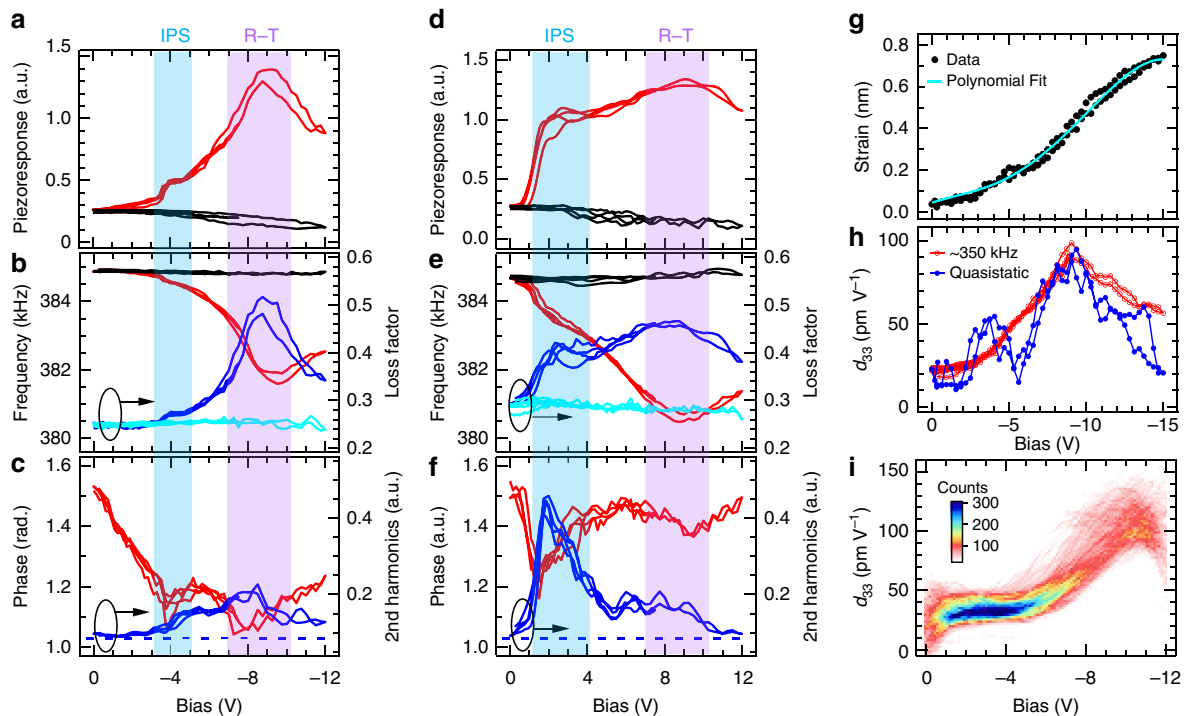


Figure 3 | Unipolar BEPS switching loops of 50 nm BFO/STO. (a–f) Unipolar BEPS loops acquired under negative (a–c) and positive (d–f) tip biases at the same location. The on-field loops are in red/blue and the off-field loops in black/cyan. Light blue and purple shadowed areas are guides to eyes indicating the in-plane switching (IPS) and $\mathbf{R} - \mathbf{T}$ transition regions, respectively. Dashed lines in c,f denote the second harmonics response signal noise floor. (g,h) Single-point strain curves (g) and its derivative (that is, static d_{33}) loops versus corresponding on-field piezoresponse loops (h). (i) Histogram of the static d_{33} loops calculated from 40×40 strain curves acquired over a $1 \times 1 \mu\text{m}^2$ region, via a 6th-order polynomial fitting to the measured data as illustrated in g. a.u., arbitrary unit.

mapping data set of strain curves based on their polynomial fits (for the noise reduction purpose; Fig. 3g). The peak d_{33} of these loops distributes over 100 – 130 pC/N, apparently comparable to that attained in mixed-phase BFO films⁷.

Effects of the complex domain structure. We have shown that the kinetic interaction between polarization switching and the R–T transition, well within the domain interior, causes characteristic asymmetry and hysteresis in the elastic softening patterns of the BFO. Next, we examine the effects of the heterogeneous domain structure. Figure 4a is a simulated multi-domain model evolving from random P values (only with the P_z component set positive) under the constraint of -1.5% substrate strains, closely resembling those observed PFM domain patterns. Negative tip biases were applied on a number of surface positions, and the resultant P–V curves for selected points are shown in Fig. 4b. As can be seen, the R–T transition starts earlier on domain walls or junctions than in the domain interior with up to ~ 2 V difference, and consequently, at the same bias the nascent T-phase is more visible on the resultant domain configuration for those ‘easier’ regions (not shown). Examination of the pristine strain state (Fig. 4c) reveals that those ‘easiest’ regions (for example, p6 and p7) are associated with larger local in-plane compressive strains (than -1.5% , the homogeneous value) as well as larger out-of-plane tensile strains; that is, they are closer to the T-phase originally. Across these walls, the polarization vector aligns tail-to-tail leading to an accumulation of bound charge, in agreement with an earlier microscopic observation of T-like structure near the charged domain walls in R-BFO⁴⁹. Note also

that the R–T transition is slightly easier even on the domain walls with reduced in-plane strains (*c.f.* p3 and p1) suggesting additional roles of domain walls in promoting the T-phase growth kinetics.

To confirm these modelling results experimentally, high-resolution BEPS mapping was performed over a typical domain junction, as shown in Fig. 4d, where the domain wall orientations are inferred from the measured PFM images based on the established domain geometry rules³⁷. This junction may well correspond to the p6 region in Fig. 4a, and here a narrow stripe of downwards polarized domain running parallel to the (100)-domain wall is observed to have formed to partially compensate the high-density negative polarization charge nearby. Around such locally stress/charge-concentrated domain walls, the higher measured peak softening $\Delta f_{c,r}$ (Fig. 4f) implies faster T-phase growth kinetics than that of the remaining region, consistent with the modelling results. The peak on-field piezoresponse also shows similar contrast in correlation with the elastic softening effect (Fig. 4e); however, this contrast is not fully disclosed in the zero-bias piezoresponse (not shown) as equivalently obtained in static PFM imaging.

Discussion

For our BEPS measurement geometry, the vertical and torsional contact mode involves the Y and G moduli, respectively, of the (001)-BFO thin film, corresponding to its elastic compliance or stiffness tensors^{50,51}: $Y_{[001]} = s_{11}^{-1} = [(c_{11} - c_{12})(c_{11} + 2c_{12})]/(c_{11} + c_{12})$ and $G = [2(s_{11} - s_{12})]^{-1} = (c_{11} - c_{12})/2$. Thus, their concomitant anomalies under E-fields appear most likely to be

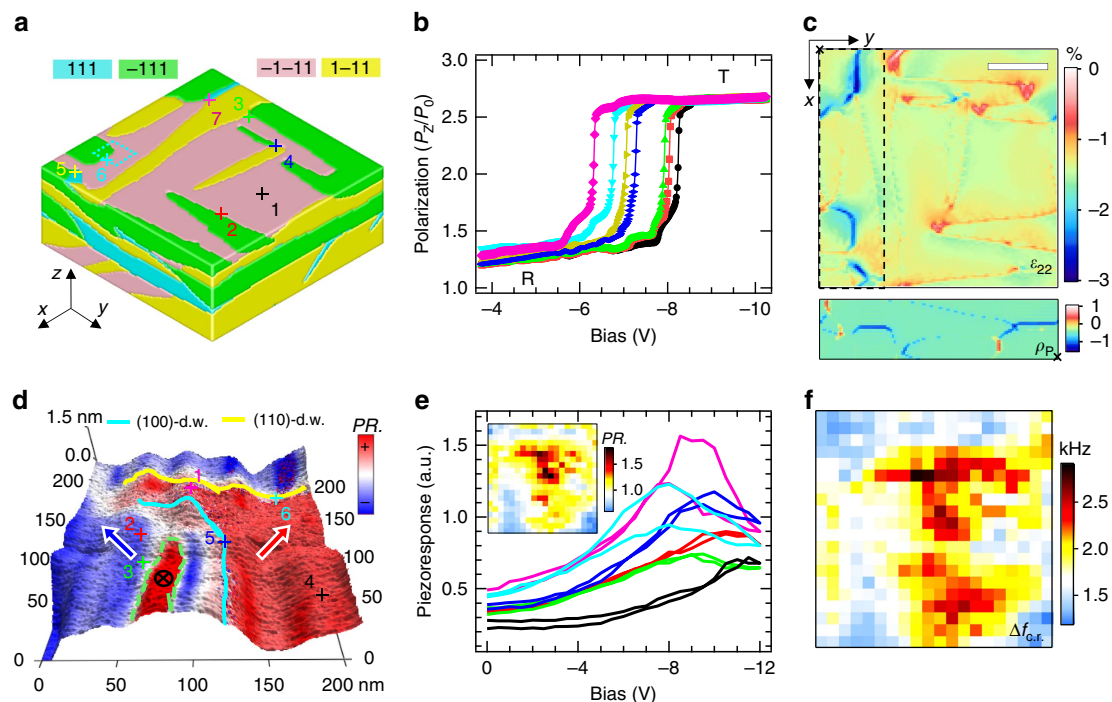


Figure 4 | Effects of the complex domain structure of BFO. (a) A phase-field simulated four-variant domain structure model (size: $128 \times 128 \times 50 \text{ nm}^3$) for R-phase BFO/STO thin films. (b) Calculated bias evolution of local polarization component P_z underneath the tip, at various surface positions marked by the crosses in a and color-coded accordingly. (c) Distribution profiles of the in-plane strain component ϵ_{22} and polarization charge ρ_p (only for the dashed-line enclosed region; unit: 10^9 C m^{-3}) for the pristine domain structure. Scale bar, 32 nm. (d) Lateral PFM domain image ($200 \times 200 \text{ nm}^2$) of a domain junction region, on which a 20×20 BEPS mapping data set was acquired. Thick arrows denote the in-plane P vectors; the whole region has an upwards out-of-plane P direction except for a stripe region enclosed by green dashed lines. The cyan and yellow lines denote the surface traces of (100)- and (101)-domain walls, respectively. (e) Selected on-field piezoresponse loops acquired at the positions marked in d and color-coded accordingly; a map of the maximum piezoresponse is shown in the inset. (f) Map of the derived maximum resonance frequency shift, $\Delta f_{c,r}$, a.u., arbitrary unit.

driven by $(c_{11} - c_{12})$. Softening of this elastic constant has been known to signify lattice instabilities against tetragonal shear strains (that is, pointing to the **R** – **T** transition here), common for many displacive ferroic systems as exemplified by Pb-based perovskite relaxors^{11,46}. For instance, an entire softened acoustic phonon branch propagating along [110] (with [1–10] transverse polarization), controlled by the $(c_{11} - c_{12})$ mode, was observed in near-MPB **R**-phase $\text{Pb}(\text{Zn}_{1/3}\text{Nb}_{2/3})\text{O}_3 - 4.5\%\text{PbTiO}_3$ coinciding with its colossal piezoelectricity⁵². Enhanced thermal diffuse scattering as a clue for Γ -point phonon softening was also observed in BFO approaching to an E-field-driven **R** – **T** transition⁵³. It is noteworthy that structurally the T-BFO stabilized on LaAlO_3 exhibits a large distortion of the oxygen octahedron and loss of its rotation pattern in **R**-BFO^{8,43,54}, implying that this transition involves multiple lattice instabilities at the *R/M*-points. These zone-boundary antiferrodistortive modes, in fact, have been argued based on first-principle calculations to be the primary order parameter, as opposed to the Γ -point polar mode, for the **R** – **T** transition of strained BFO⁵⁵, posing it as a (pseudo-)proper ferroelastic transition. All these complex transition characters clearly have effects on the strain-coupling mechanism and elastic softening dynamics of BFO. Given a dearth of experimental lattice dynamics studies of the system thus far, we leave this as an inconclusive account of the detailed microscopic picture behind our observations; nevertheless, these results *per se* are clearly a direct measure of soft acoustic modes of BFO in the long wavelength limit.

This giant elastic softening effect of BFO coupled with non-hysteretic and reasonably low-loss characteristics suggests its usefulness in tunable microwave electroacoustic devices^{3,56–59}. Currently, the prevailing materials for these applications are based on paraelectric-phase $(\text{Ba,Sr})\text{TiO}_3$ with incipient polar instability (that is, soft optic modes), while materials set in polar phases are less often considered due to unfavourable domain switching related hysteresis and loss. In both cases, frequency tunability is underlain by the soft optic phonons (and/or relaxational modes), which harden under d.c. E-fields^{56,59}, primarily leading to changes in polarization ΔP ; via an electrostrictive coupling, this ΔP shifts the elastic stiffness downwards and upwards for paraelectric and polar phases, respectively, and does so in opposite ways to their electromechanical properties³. By contrast, the utilization of BFO here is conceptually different in that the acoustic modes of BFO soften near a successive ferroelectric/–elastic phase transition that is likely triggered by optic soft modes coupled to applied E-fields. Simple estimation suggests that 20 – 30% ΔY , as we typically observed, can lead to over 10% frequency tunability in a thickness extension-mode resonator. This factor, compared with the state-of-art $\sim 1 - 4\%$ values attained in $(\text{Ba,Sr})\text{TiO}_3$ (refs 3,58), would make it highly rewarding to explore the demonstration in prototype devices. We further note that the **R** – **T** phase instabilities of BFO can be tailored via epitaxial strain⁶⁰, chemical doping⁶¹ and possibly a more radical route of superlattice design⁵⁹, and combinations thereof, offering practical ways to circumvent low dielectric strength issues known for BFO⁵³.

To realize such functionalities of BFO and materials alike, in turn, requires a deep survey of the structure – dynamics correlation at pertinent length levels thus providing feedback for materials design. The approach here, we demonstrated, effectively bridges the structural gap between the atomic lattice and mesoscopic domains; the complex dynamic interplay between intrinsic order parameters and structural heterogeneity within these length scales necessitates probing their elasticity/polarization dynamics as an integral part. This approach can be immediately extended to other MPB ferroelectric systems.

Beyond this, given the ubiquitous elastic anomalies near phase transitions of diverse nature in solid-state materials, our study may also furnish far-reaching clues as to examining their dynamics from the nanoscale under locally or globally applied driving forces (for example, temperature and magnetic fields).

Methods

Sample fabrication. 50 nm BFO thin films were grown using a reflection high-energy electron diffraction-assisted pulsed laser deposition system on pretreated TiO_2 -terminated STO(001) substrates, with 5 nm per 13 unit-cell $\text{La}_{0.7}\text{Sr}_{0.3}\text{MnO}_3$ as bottom electrodes. The BFO and $\text{La}_{0.7}\text{Sr}_{0.3}\text{MnO}_3$ layers were grown at 690 °C at an oxygen partial pressure of 100 and 300 mTorr, respectively. The laser repetition frequency and energy were set to 1 Hz per 1.5 J cm^{-2} for the growth of $\text{La}_{0.7}\text{Sr}_{0.3}\text{MnO}_3$ and 3 Hz per 2.5 J cm^{-2} for BFO. The crystal structure of the films was examined using X-ray (15.499 keV) diffraction at Beamline 33-BM-C, Advanced Photon Source, Argonne National Laboratory.

PFM Experiments. PFM was carried out in ambient environment on a commercial atomic force microscope (Cypher AFM, Asylum Research), equipped with a home-developed band-excitation controller based on a National Instruments PXIe-6124 data acquisition card operating in Labview/Matlab software. Pt/Ir-coated conductive Si probes with medium stiffness $k = 2 - 5 \text{ N m}^{-1}$ were used in contact mode with loading forces set at $\sim 300 \text{ nN}$. The vertical sensitivities of cantilevers were determined from acquired force–distance curves. In BEPS, contact resonance spectra of the tip–sample junction were electrically excited using chirp-type band-excitation signals, typically with 1 V a.c. amplitude, 4–8 ms time length and 40 kHz bandwidth bracketing the resonance peaks, and were captured as a function of d.c. switching waveforms within up to $\pm 16 \text{ V}$ bias windows. Measured spectra were fitted to a simple harmonic oscillator model³⁴ to decouple intrinsic piezoresponse, resonance frequency (ω_c) and Q factor with great veracity. The latter two quantities encode near-surface elastic information of the sample; thereby contact resonance plays another important role in BEPS besides signal enhancement. BEPS mapping was performed on grids of points evenly spaced on predefined scan regions. Conduction current was monitored with a current amplifier (DLPCA-200, Femto).

Phase-field modelling. Temporal, three-dimensional spatial evolution of the ferroelectric polarization of the BFO films is modelled by numerically solving the time-dependent Landau–Ginzburg–Devonshire (LGD) equations⁶²,

$$\frac{\partial P_i(x, t)}{\partial t} = -L \frac{\delta F}{\delta P_i(x, t)}, \quad i = 1, 2, 3, \quad (1)$$

in which P_i is the polarization vector, x is the spatial position, t is the time, L is the kinetic coefficient related to the domain wall mobility, F is the total free energy,

$$F = \int_V [f_{\text{lan}}(P_i) + f_{\text{grad}}(P_{ij}) + f_{\text{elas}}(P_i, \epsilon_{ij}) + f_{\text{elec}}(P_i, E_i)] dV \quad (2)$$

in which $f_{\text{lan}}(P_i)$, $f_{\text{grad}}(P_{ij})$, $f_{\text{elas}}(P_i, \epsilon_{ij})$ and $f_{\text{elec}}(P_i, E_i)$ represent the LGD free-energy density, gradient-energy density, elastic-energy density and electrostatic-energy density, respectively. Detailed description and analytic expressions for these energy terms can be found in literature⁶³; in particular, here we adopted an eighth-order LGD free energy expansion for BFO. Isotropic gradient energy coefficients $G_{ii} = 0.3$ and relative dielectric constant $\kappa_{ii} = 50$ were assumed. All the energy coefficients of BFO and detailed model parameters are provided in Supplementary Table 2. Equation (1) was solved by a semi-implicit spectral method⁶⁴ using a realistic three-dimensional geometry sampled on a fine grid mesh of $128\Delta x_1 \times 128\Delta x_2 \times 64\Delta x_3$, where the grid size $\Delta x = 1.0 \text{ nm}$. The film and substrate thickness are $50\Delta x$ and $10\Delta x$, respectively. Periodic boundary conditions were applied for the in-plane directions (x_1 and x_2); the top film surface is assumed to be stress-free, while the bottom surface of BFO is coherently strained by the substrate⁶³. Electric biases were incrementally applied via the tip function described in the text.

References

1. Scott, J. F. Applications of modern ferroelectrics. *Science* **315**, 954–959 (2007).
2. Uchino, K. *Ferroelectric Devices* 2nd edn (CRC Press, 2009).
3. Gevorgian, S., Tagantsev, A. & Vorobiev, A. K. *Tunable Film Bulk Acoustic Wave Resonators* (Springer, 2013).
4. Damjanovic, D. Contributions to the piezoelectric effect in ferroelectric single crystals and ceramics. *J. Am. Ceram. Soc.* **88**, 2663–2676 (2005).
5. Jaffe, B., Cook, W. R. & Jaffe, H. *Piezoelectric Ceramics* (Academic, 1971).
6. Lummen, T. T. A. *et al.* Thermotropic phase boundaries in classic ferroelectrics. *Nat. Commun.* **5**, 3172 (2014).
7. Park, S. E. & Shrout, T. R. Ultrahigh strain and piezoelectric behavior in relaxor based ferroelectric single crystals. *J. Appl. Phys.* **82**, 1804–1811 (1997).

8. Zeches, R. J. *et al.* A strain-driven morphotropic phase boundary in BiFeO₃. *Science* **326**, 977–980 (2009).
9. Zhang, J. X. *et al.* Large field-induced strains in a lead-free piezoelectric material. *Nat. Nanotechnol.* **6**, 98–102 (2011).
10. Ahart, M. *et al.* Origin of morphotropic phase boundaries in ferroelectrics. *Nature* **451**, 545–548 (2008).
11. Wu, Z. G. & Cohen, R. E. Pressure-induced anomalous phase transitions and colossal enhancement of piezoelectricity in PbTiO₃. *Phys. Rev. Lett.* **95**, 037601 (2005).
12. Noheda, B. *et al.* Polarization rotation via a monoclinic phase in the piezoelectric 92%PbZn_{1/3}Nb_{2/3}O₃-8%PbTiO₃. *Phys. Rev. Lett.* **86**, 3891–3894 (2001).
13. Christen, H. M., Nam, J. H., Kim, H. S., Hatt, A. J. & Spaldin, N. A. Stress-induced R-M_A-M_C-T symmetry changes in BiFeO₃ films. *Phys. Rev. B* **83**, 144107 (2011).
14. Fu, H. & Cohen, R. E. Polarization rotation mechanism for ultrahigh electromechanical response in single-crystal piezoelectrics. *Nature* **403**, 281–283 (2000).
15. Xu, R., Karthik, J., Damodaran, A. R. & Martin, L. W. Stationary domain wall contribution to enhanced ferroelectric susceptibility. *Nat. Commun.* **5**, 3120 (2014).
16. Zhang, Q. M., Wang, H., Kim, N. & Cross, L. E. Direct evaluation of domain wall and intrinsic contributions to the dielectric and piezoelectric response and their temperature dependence on lead zirconate titanate ceramics. *J. Appl. Phys.* **75**, 454–459 (1994).
17. Sluka, T., Tagantsev, A. K., Damjanovic, D., Gureev, M. & Setter, N. Enhanced electromechanical response of ferroelectrics due to charged domain walls. *Nat. Commun.* **3**, 748 (2012).
18. Jesse, S., Lee, H. N. & Kalinin, S. V. Quantitative mapping of switching behavior in piezoresponse force microscopy. *Rev. Sci. Instrum.* **77**, 073702 (2006).
19. Morozovska, A. N. *et al.* Piezoresponse force spectroscopy of ferroelectric-semiconductor materials. *J. Appl. Phys.* **102**, 114108 (2007).
20. Jesse, S. *et al.* Direct imaging of the spatial and energy distribution of nucleation centres in ferroelectric materials. *Nat. Mater.* **7**, 209–215 (2008).
21. Kalinin, S. V., Morozovska, A. N., Chen, L. Q. & Rodriguez, B. J. Local polarization dynamics in ferroelectric materials. *Rep. Prog. Phys.* **73**, 056502 (2010).
22. Balke, N. *et al.* Deterministic control of ferroelastic switching in multiferroic materials. *Nat. Nanotechnol.* **4**, 868–875 (2009).
23. Fujino, S. *et al.* Combinatorial discovery of a lead-free morphotropic phase boundary in a thin-film piezoelectric perovskite. *Appl. Phys. Lett.* **92**, 202904 (2008).
24. Wang, J. *et al.* Epitaxial BiFeO₃ multiferroic thin film heterostructures. *Science* **299**, 1719–1722 (2003).
25. Seidel, J. *et al.* Conduction at domain walls in oxide multiferroics. *Nat. Mater.* **8**, 229–234 (2009).
26. Catalan, G. & Scott, J. F. Physics and applications of bismuth ferrite. *Adv. Mater.* **21**, 2463–2485 (2009).
27. Lejman, M. *et al.* Giant ultrafast photo-induced shear strain in ferroelectric BiFeO₃. *Nat. Commun.* **5**, 4301 (2014).
28. Heron, J. T. *et al.* Deterministic switching of ferromagnetism at room temperature using an electric field. *Nature* **516**, 370–373 (2014).
29. Mazumdar, D. *et al.* Nanoscale switching characteristics of nearly tetragonal BiFeO₃ thin films. *Nano Lett.* **10**, 2555–2561 (2010).
30. Zhang, J. *et al.* A nanoscale shape memory oxide. *Nat. Commun.* **4**, 2768 (2013).
31. Li, Y.-J. *et al.* Mechanical switching of nanoscale multiferroic phase boundaries. *Adv. Funct. Mater.* **25**, 3405–3413 (2015).
32. Heo, Y., Jang, B.-K., Kim, S. J., Yang, C.-H. & Seidel, J. Nanoscale mechanical softening of morphotropic BiFeO₃. *Adv. Mater.* **26**, 7568–7572 (2014).
33. Cheng, C.-E. *et al.* Revealing the flexoelectricity in the mixed-phase regions of epitaxial BiFeO₃ thin films. *Sci. Rep.* **5**, 8091 (2015).
34. Jesse, S., Kalinin, S. V., Proksch, R., Baddorf, A. P. & Rodriguez, B. J. The band excitation method in scanning probe microscopy for rapid mapping of energy dissipation on the nanoscale. *Nanotechnology* **18**, 435503 (2007).
35. Scott, J. F., Salje, E. K. H. & Carpenter, M. A. Domain wall damping and elastic softening in SrTiO₃: Evidence for Polar Twin Walls. *Phys. Rev. Lett.* **109**, 187601 (2012).
36. Yu, P. *et al.* Interface control of bulk ferroelectric polarization. *Proc. Natl Acad. Sci. USA* **109**, 9710–9715 (2012).
37. Streiffer, S. K. *et al.* Domain patterns in epitaxial rhombohedral ferroelectric films. I. Geometry and experiments. *J. Appl. Phys.* **83**, 2742–2753 (1998).
38. Li, Q. *et al.* Probing local bias-induced transitions using photothermal excitation contact resonance atomic force microscopy and voltage spectroscopy. *ACS Nano* **9**, 1848–1857 (2015).
39. Li, Q. *et al.* Fully-inverted piezoresponse hysteresis loops mediated by charge injection in 0.29Pb(In_{1/2}Nb_{1/2})O₃-0.44Pb(Mg_{1/3}Nb_{2/3})O₃-0.27PbTiO₃ single crystals. *Appl. Phys. Lett.* **98**, 092908 (2011).
40. Rabe, U. in *Applied Scanning Probe Methods II*. (eds Bhushan, Bharat & Fuchs, Harald) Ch. 2 (Springer, 2006).
41. Doig, K. I. *et al.* Coherent magnon and acoustic phonon dynamics in tetragonal and rare-earth-doped BiFeO₃ multiferroic thin films. *Phys. Rev. B* **88**, 094425 (2013).
42. Kalinin, S. V. & Bonnell, D. A. Imaging mechanism of piezoresponse force microscopy of ferroelectric surfaces. *Phys. Rev. B* **65**, 125408 (2002).
43. Zhang, J. X. *et al.* Microscopic Origin of the giant ferroelectric polarization in tetragonal-like BiFeO₃. *Phys. Rev. Lett.* **107**, 147602 (2011).
44. Dong, H., Chen, C., Wang, S., Duan, W. & Li, J. Elastic properties of tetragonal BiFeO₃ from first-principles calculations. *Appl. Phys. Lett.* **102**, 182905 (2013).
45. Damjanovic, D. Comments on origins of enhanced piezoelectric properties in ferroelectrics. *IEEE Trans. Ultrason. Ferroelectr. Freq. Control* **56**, 1574–1585 (2009).
46. Carpenter, M. A. & Salje, E. K. H. Elastic anomalies in minerals due to structural phase transitions. *Eur. J. Mineral.* **10**, 693–812 (1998).
47. Vasudevan, R. K. *et al.* Unraveling the origins of electromechanical response in mixed-phase bismuth ferrite. *Phys. Rev. B* **88**, 020402 (2013).
48. Trolrier-McKinstry, S., Bassiri Gharb, N. & Damjanovic, D. Piezoelectric nonlinearity due to motion of 180° domain walls in ferroelectric materials at subcoercive fields: a dynamic poling model. *Appl. Phys. Lett.* **88**, 202901 (2006).
49. Li, L. *et al.* Atomic scale structure changes induced by charged domain walls in ferroelectric materials. *Nano Lett.* **13**, 5218–5223 (2013).
50. Drobek, T., Stark, R. W. & Heckl, W. M. Determination of shear stiffness based on thermal noise analysis in atomic force microscopy: Passive overtone microscopy. *Phys. Rev. B* **64**, 045401 (2001).
51. Nye, J. F. *Physical Properties of Crystals: Their Representation by Tensors and Matrices* (Clarendon Press, 1985).
52. Xu, G., Wen, J., Stock, C. & Gehring, P. M. Phase instability induced by polar nanoregions in a relaxor ferroelectric system. *Nat. Mater.* **7**, 562–566 (2008).
53. Chen, P. *et al.* Nonlinearity in the high-electric-field piezoelectricity of epitaxial BiFeO₃ on SrTiO₃. *Appl. Phys. Lett.* **100**, 062906 (2012).
54. Lisenkov, S., Rahmedov, D. & Bellaiche, L. Electric-field-induced paths in multiferroic BiFeO₃ from atomistic simulations. *Phys. Rev. Lett.* **103**, 047204 (2009).
55. Wojdel, J. C. & Iniguez, J. Ab initio indications for giant magnetoelectric effects driven by structural softness. *Phys. Rev. Lett.* **105**, 037208 (2010).
56. Akimov, I. A., Sirenko, A. A., Clark, A. M., Hao, J. H. & Xi, X. X. Electric-field-induced soft-mode hardening in SrTiO₃ films. *Phys. Rev. Lett.* **84**, 4625–4628 (2000).
57. Tagantsev, A. K., Sherman, V. O., Astafiev, K. F., Venkatesh, J. & Setter, N. Ferroelectric materials for microwave tunable applications. *J. Electroceram.* **11**, 5–66 (2003).
58. Vorobiev, A., Gevorgian, S., Martirosyan, N., Loffler, M. & Olsson, E. Intrinsically tunable 0.67BiFeO₃-0.33BaTiO₃ thin film bulk acoustic wave resonators. *Appl. Phys. Lett.* **101**, 232903 (2012).
59. Lee, C.-H. *et al.* Exploiting dimensionality and defect mitigation to create tunable microwave dielectrics. *Nature* **502**, 532–536 (2013).
60. Schlom, D. G. *et al.* Elastic strain engineering of ferroic oxides. *MRS Bull.* **39**, 118–130 (2014).
61. Diéguez, O. & Íñiguez, J. First-principles investigation of morphotropic transitions and phase-change functional responses in BiFeO₃-BiCoO₃ multiferroic solid solutions. *Phys. Rev. Lett.* **107**, 057601 (2011).
62. Li, Y. L., Hu, S. Y., Liu, Z. K. & Chen, L. Q. Effect of substrate constraint on the stability and evolution of ferroelectric domain structures in thin films. *Acta Mater.* **50**, 395–411 (2002).
63. Chen, L.-Q. Phase-field method of phase transitions/domain structures in ferroelectric thin films: a review. *J. Am. Ceram. Soc.* **91**, 1835–1844 (2008).
64. Chen, L. Q. & Shen, J. Applications of semi-implicit Fourier-spectral method to phase field equations. *Comput. Phys. Commun.* **108**, 147–158 (1998).

Acknowledgements

This work was supported by the US DOE, Basic Energy Sciences, Materials Sciences and Engineering Division through the Office of Science Early Career Research Program (N.B., Q.L.). The experiments were performed at the Center for Nanophase Materials Sciences, which is sponsored at ORNL by the Scientific User Facilities Division, Office of Basic Energy Sciences, US DOE. P.Y. was supported by the National Basic Research Program of China (Grant No. 2015CB921700) and National Natural Science Foundation of China (Grant No. 11274194). L.Q.C. was supported by the US DOE, Office of Basic Energy Sciences, Materials Sciences and Engineering Division under Award No. DE-FG02-07ER46417. F.X. was supported by NSF MRSEC under Grant No. DMR-1420620. Use of the Advanced Photon Source, an Office of Science User Facility operated for the US DOE Office of Science by Argonne National Laboratory, was supported by the US DOE under Contract No. DE-AC02-06CH11357. Q.L. acknowledges helpful discussions with Michael A. Carpenter and Anna N. Morozovska.

Author contributions

Q.L. conceived the study, performed PFM, analysed the results and wrote the article. Y.C. designed and performed phase-field modelling with input from L.Q.C. and F.X. derived the LGD energy coefficients. P.Y. provided the materials. N.L. performed XRD. A.T. performed cantilever dynamics calculation. R.K.V., N.L. and P.M. discussed the results. N.B. and S.V.K. supervised the study and co-wrote the article. All authors commented on the manuscript.

Additional information

Supplementary Information accompanies this paper at <http://www.nature.com/naturecommunications>

Competing financial interests: The authors declare no competing financial interests.

Reprints and permission information is available online at <http://npg.nature.com/reprintsandpermissions/>

How to cite this article: Li, Q. *et al.* Giant elastic tunability in strained BiFeO₃ near an electrically induced phase transition. *Nat. Commun.* 6:8985 doi: 10.1038/ncomms9985 (2015).



This work is licensed under a Creative Commons Attribution 4.0 International License. The images or other third party material in this article are included in the article's Creative Commons license, unless indicated otherwise in the credit line; if the material is not included under the Creative Commons license, users will need to obtain permission from the license holder to reproduce the material. To view a copy of this license, visit <http://creativecommons.org/licenses/by/4.0/>